CrossMark

Preparation, characterization and X-ray attenuation property of Gd$_2$O$_3$-based nanocomposites

Sangeetha Jayakumar[1] · T. Saravanan[2] · John Philip[1]

Abstract In an attempt to develop an alternate to lead-based X-ray shielding material, we describe the X-ray attenuation property of nanocomposites containing Gd$_2$O$_3$ as nanofiller and silicone resin as matrix, prepared by a simple solution-casting technique. Gd$_2$O$_3$ nanoparticles of size 30 and 56 nm are used at concentrations of 25 and 2.5 wt%. The nanoparticles and the nanocomposites are characterized using X-ray diffraction (XRD) studies, small angle X-ray spectroscopy (SAXS), thermogravimetric analysis (TGA), differential scanning calorimetry (DSC) and atomic force microscopy (AFM). The X-ray attenuation property of nanocomposites, studied using an industrial X-ray unit, shows that nanocomposites containing nanoparticles of size 56 nm (G2) exhibit better attenuation than nanocomposites containing nanoparticles of size 30 nm (G1), which is attributed to the greater interfacial interaction between the G2 nanofillers and silicone matrix. In the case of nanocomposites containing G1 nanoparticles, the interfacial interaction between the nanofiller and the matrix is so weak that it results in pulling out of nanofillers, causing voids in the matrix, which act as X-ray transparent region, thereby reducing the overall X-ray attenuation property of G1 nanocomposites. This is further corroborated from the AFM images of the nanocomposites. The weight loss and heat flow curves of pure silicone matrix and the nanocomposites containing Gd$_2$O$_3$ nanoparticles of size 30 and 56 nm show the degradation of silicone resin, due to chain scission, between 403 and 622 °C. The same onset temperature (403 °C) of degradation of matrix with and without nanoparticles shows that the addition of nanofillers to the matrix does not deteriorate the thermal stability of the matrix. This confirms the thermal stability of nanocomposites. Therefore, our study shows that nanocomposites containing G2 nanoparticles are potential candidates for the development of X-ray opaque fabric material.

Keywords X-ray attenuation · Gd$_2$O$_3$ · RTV silicone resin · Nanocomposite

Introduction

Nanomaterials are drawing great attention as an alternate to lead-based radiation shielding material, as lead is a potent occupational toxin that exhibits several toxicological manifestations such as persistent vomiting, encephalopathy, lethargy, delirium, convulsions and coma (Flora et al. 2012; Kiran 2015; La et al. 2016). The lead toxicity mechanism involves an increased generation of reactive oxygen species (ROS), depletion of antioxidant reserve due to the binding of lead to sulfhydryl groups of antioxidants, lipid peroxidation, haemoglobin oxidation and ion substitution such as replacement of Ca^{2+}, Mg^{2+} and Na^+ (Flora et al. 2012; La et al. 2016). The radiation attenuation property of nanomaterials has been explored extensively in the past to replace the existing toxic lead-based materials for radiation protection (Abdulla et al. 2015; Adliene et al. 2015; Aral et al. 2016; Fujimori et al. 2011; Kim et al.

✉ John Philip
philip@igcar.gov.in

1 SMART Materials Section, Corrosion Science and Technology Division, Metallurgy and Materials Group, Indira Gandhi Centre for Atomic Research, HBNI, Kalpakkam 603102, India

2 Inspection Technology Section, Non-Destructive Evaluation Division, Metallurgy and Materials Group, Indira Gandhi Centre for Atomic Research, HBNI, Kalpakkam 603102, India

2015). For example, Fontainha et al. (2016) have demonstrated a 60% attenuation of X-rays of energy 40 keV by the nanocomposites of poly(vinylidene fluoride–trifluoroethylene) and zirconia nanoparticles. Li et al. (2016) have described the fabrication of polymethyl methacrylate and multiwalled carbon nanotube-based nanocomposites. In their study, the nanocomposites are found to attenuate protons and are 18–19% lighter than their aluminium counterparts, generating up to 5% less secondary neutrons. Thibeault et al. (2015) have discussed the application of various nanomaterials such as single-walled carbon nanotube, multiwalled carbon nanotube, boron nitride nanotubes, tungsten nanoparticles and gold nanofoams for protection against galactic cosmic radiation (GCR), solar particle event (SPEs) and neutrons obtained from GCR–SPEs interaction. Gadolinium oxide nanoparticle is shown to attenuate X-rays and gamma rays (Roux et al. 2010). Gadolinium oxide is a sesquioxide which exists in two crystalline forms depending on the temperature, namely, cubic structure (stable at room temperature) and the monoclinic structure (> 1250 °C) (Jamnezhad and Jafari 2016). Monoclinic and cubic Gd_2O_3 nanoparticles are paramagnetic in nature and become antiferromagnetic at a Neel temperature of 17.2 K (Jamnezhad and Jafari 2016). Gd^{3+} ion in gadolinium oxide possesses seven unpaired electrons in the 4f orbital with an electron spin of 7/2 (Ahren et al. 2012). It exhibits a long electronic relaxation time of 10^{-8}–10^{-9} s, with a large magnetic moment (Gayathri et al. 2015). Gd_2O_3 nanoparticles find applications in bioimaging (when tagged with fluorescent dyes) (Dosev et al. 2006), in magnetic resonance imaging as contrast agent (Fortin et al. 2007; Khan et al. 2014) and in drug delivery (Khan et al. 2014). They are also used as neutron convertors in imaging plate neutron detector (Bhattacharyya and Agrawal 1995; Gunduz and Uslu 1996; Khan et al. 2014), as additives in UO_2 fuel rods (Gunduz and Uslu 1996; Khan et al. 2014), in ZrO_2 to enhance its toughness (Bhattacharyya and Agrawal 1995; Chen 1996; Khan et al. 2014), as a radiosensitizer (Duc et al. 2011; Miladi et al. 2015; Mowat et al. 2011; Rancoule et al. 2016; Rima et al. 2013), as a catalyst (Hussein 1994; Perevalov et al. 2014) and dopants for laser (Perevalov et al. 2014) and colourants (Perevalov et al. 2014) for special glasses.

Wang et al. (Wang et al. 2015a) have prepared water-dispersible nanocomposite of Gd_2O_3 and graphene oxide that was found to exhibit an enhanced MRI T1 relaxivity than the commercially available MRI T1 contrast agents. Zhou et al. (Zhou et al. 2017) have described the synthesis of albumin-conjugated Gd_2O_3-based photosensitizers. The authors have demonstrated an enhanced MRI contrast and photothermal effect by Gd_2O_3-based photosensitizers. Kusiak and Zaborski (2012) have studied the X-ray absorption properties of nanocomposites containing

nanoparticles such as Gd_2O_3, Bi_2O_3, WO_2 and antimony oxide at various concentrations. In their study, nanocomposites containing Bi_2O_3, Gd_2O_3, WO_3 and Sb_2O_3 at a concentration of 50, 30, 20 and 20 phr, respectively, are found to strongly absorb X-rays. Stefancikova et al. (2016) have studied the role of gadolinium-based nanoparticles as radiosensitizers and have shown that the radiosensitization mediated by gadolinium-based nanocomposite is a cytoplasmic event, independent of nuclear DNA damage.

A number of studies have been carried out to evaluate the X-ray attenuation property of Gd_2O_3 nanoparticles and Gd_2O_3-based nanocomposites (La et al. 2016; Mao et al. 2015; Wang et al. 2015b). Gadolinium ion is shown to accumulate in the brain, bone and kidneys (Ramalho et al. 2016; Rogosnitzky and Branch 2016). Due to the size similarity of Gd^{3+} to Ca^{2+} ions, Gd^{3+} ions could bind to enzymes with Ca^{2+} binding sites and inactivate them. Gd^{3+} ions could also affect the voltage-gated calcium channels, thereby resulting in adverse biological effects (Ramalho et al. 2016; Rogosnitzky and Branch 2016). Hence, gadolinium-based chelates and stable compounds are used for biological applications (Rogosnitzky and Branch 2016), instead of gadolinium ions. Gadolinium-based chelates are widely used as MRI contrast agents (Rogosnitzky and Branch 2016), where gadobenate, gadobutrol and gadodiamide are some of the US Food and Drug Administration (FDA)-approved contrast agents for MRI (Rogosnitzky and Branch 2016).

Sambhudevan et al. (2017) have prepared natural rubber-based nanocomposites containing methacrylic acid-modified Gd_2O_3 nanoparticles that are found to exhibit X-ray attenuation property. Wang et al. (Wang et al. 2015b) have described the preparation of nanocomposites with polyether ether ketone as the matrix and untreated Gd_2O_3 and sulfonated polyether ether ketone-coated Gd_2O_3 as nanofillers. In their study, the nanocomposites are found to exhibit X-ray shielding property against X-rays of energy 40–80 keV. Li et al. (Li et al. 2017) have prepared epoxy resin-based nanocomposites containing gadolinium oxide of size 100 nm and 6 μm. The authors have studied the gamma ray attenuation property of these nanocomposites and have shown an enhanced shielding property of nano-Gd_2O_3 nanocomposite than micro-Gd_2O_3 composite. Mao et al. (2015) have studied the X-ray attenuation property of rubber nanocomposite containing Gd_2O_3 nanoflakes which is found to exhibit X-ray attenuation property and a high tensile strength. Ambika et al. (2016) have studied the gamma shielding property of unsaturated polyester resin-based nanocomposite containing bismuth oxide nanoparticles, with a shielding ability comparable to that of barite at low energies of gamma rays. Scuderi et al. (2006) have studied the radiation protection efficacy of commercially available non-lead-based radiation protective

garments such as Xenolite, EarthSafe and Demron against X-rays of energy 60–120 keV. In their study, Demron is found to exhibit better attenuation than EarthSafe and Xenolite. Akbulut et al. (2015) have studied the radiation shielding property of clay–white cement, clay–silica fume, gypsum, gypsum–silica fume, cement, white cement, cement–silica fume, white cement–gypsum, white cement–silica fume, red mud–silica fume, silica fume and red mud samples against gamma rays. In their study, clay–white cement mixture was found to be superior to other studied samples. In our previous study (Jayakumar et al. 2017), we have successfully demonstrated the attenuation property of α-Bi_2O_3-, β-Bi_2O_3- and Bi-based nanocomposites, where, β-Bi_2O_3-based nanocomposites were found to attenuate X-rays, in diagnostic range, better than α-Bi_2O_3- and Bi-based nanocomposites.

The present study focuses on the development of flexible and stable nanocomposites of vulcanized silicone resin as matrix, reinforced with Gd_2O_3 nanoparticles as nanofillers. A study on the effect of the size of Gd_2O_3 nanoparticles and its concentration on the thermal stability and X-ray attenuation property was also performed.

Materials and methods

Gadolinium oxide (Otto Chemie) of size 30 nm (G1) and 56 nm (G2) was used in this study without any further modification. Room temperature X-ray diffraction (XRD) and small angle X-ray scattering (SAXS) studies were performed, to determine the size of the nanoparticles, using Rigaku Ultima IV X-ray diffractometer. The diffraction pattern was obtained for 2θ values of 20°–80° using Cu K_α X-rays, with Bragg–Brentano geometry. Each measurement was obtained at a scan rate of 2°/min with a step interval of 0.02°. The crystallite size (d) of the nanoparticles was calculated using Scherrer formula, as given below:

$$d = \frac{k\lambda}{\beta \cos \theta}, \tag{1}$$

where, $k = 0.89$, $\lambda = 1.5418$ Å, β is the full width at half maxima (FWHM) of the most intense peak and θ is the Bragg angle in degrees. In SAXS measurement, the scattering intensity ($I(q)$) was measured as a function of scattering vector, $q = (4\pi \sin \theta)/\lambda$, and is fit with a spherical model given below:

$$I(q) = |\Delta\rho|^2 \left| \frac{4\pi}{q^3} \left[\sin\left(\frac{qd}{2}\right) - \frac{qd}{2}\cos\left(\frac{qd}{2}\right) \right] \right|^2, \tag{2}$$

where, d is the diameter of the particle and $\Delta\rho$ is the difference in the electron density of the particle and the medium. The average particle size was obtained from the distance distribution function.

Nanocomposite blocks were prepared using a commercially available two-component room temperature vulcanized (RTV) silicone resin and Gd_2O_3 nanoparticles of two different sizes. RTV silicone resin (Make: Anabond) consisted of Part A and Part B, with a mixing ratio of 100:5. It formed a rubber-like material on curing. Nanocomposite blocks consisting of Gd_2O_3 nanoparticles were prepared by mixing Part A and Part B of silicone resin containing 25 and 2.5 wt% of Gd_2O_3 nanoparticles, respectively. The mixture was poured onto a stainless steel mould and set for 8 h. Then, blocks of thickness $\sim$ 2.5 mm with a length and width of 3×3 cm were retrieved from the mould. Nanocomposites containing 25 and 2.5 wt% of G1 nanoparticles are referred to as G1–25 and G1–2.5, respectively. Similarly, nanocomposites containing 25 and 2.5 wt% of G2 nanoparticles are referred to as G2–25 and G2–2.5, respectively.

Thermal analysis of nanocomposites such as thermogravimetric analysis (TGA) and differential scanning calorimetry (DSC) were carried out using a thermogravimetric analyser (Mettler Toledo, LF Switzerland), in the temperature range of 30–800 °C under argon atmosphere and at a heating rate of 10 °C/min. X-ray radiography experiments were performed using a 200 MF X-ray unit (Eresco Rich-Seifert), with a focal spot size of 1.5 mm. The nanocomposite blocks were exposed to 30–60 kV X-rays for 1.75 min at a distance of 1 m from the source. The X-ray detector used was a Gd_2O_2S scintillation-based amorphous silicon (indirect type) 14-bit flat panel system (Thales FlashScan FS35), with a pixel resolution of 127 μm and an active area of 32×40 cm. Data acquisition and analysis was done using the Vj3 software. The linear attenuation coefficient and percentage attenuation of the blocks were obtained using a grey-level profile method.

Lead equivalence of the nanocomposite blocks was studied using 0.05, 0.1, 0.2, 1.5 and 3 mm-thick standard lead foil. Standard lead foils were exposed to the incident X-ray photons along with the prepared nanocomposite blocks. The grey value obtained for the standard lead foil was used to extrapolate the lead equivalence of G1–25, G1–2.5, G2–25 and G2–2.5 nanocomposite blocks. The half-value layer (HVL) of the prepared nanocomposite blocks was obtained from the linear attenuation coefficient values. The surface morphology of the nanocomposite blocks was studied using an atomic force microscope (NTEGRA PRIMA, NT-MDT, Russia) in contact mode, in which an Si_3N_4 cantilever of tip radius 20 nm was used. The average surface roughness was obtained from the AFM topography images, using simple statistics. The surface roughness is calculated using a roughness 3-D method which characterizes features of a surface in three-dimensional (3D) geometrical space, described by a two-variable function $Z(x, y)$ over a defined domain of the XY plane.

Therefore, the 3-D roughness method, which is in accordance with ASME B46.1-2009 and ISO 25178-2:2012 standards, calculates the standard statistical parameters of the source data $Z(xi, yi)$ (average value, rms deviation, minimum, maximum, etc.) and provides a peak distribution (cumulative distribution) and histogram (distribution density) of source data. In this study, the amount of sampling used is 65,536 data points with a sampling area of 899.87 μm^2. The nanocomposites are further cleaved to study the morphology of the cross section using AFM. The scanning electron microscopy (SEM) image of the top surface and the cleaved cross section of the G2–25 nanocomposite block was also obtained using Phenom scanning electron microscope in environmental mode, with an accelerating voltage of 10 kV.

Results and discussion

Figure 1 shows the XRD pattern of (a) G1 and (b) G2 nanoparticles. Both G1 and G2 nanoparticles exhibit the diffraction peaks corresponding to Bragg reflections from (211), (222), (400), (411), (431), (440), (611), (622), (444) and (662) crystal planes, which can be indexed to the cubic structure of Gd_2O_3 nanoparticles (JCPDS Card No.01-073-6280). This is in good agreement with the literature (Abdullah et al. 2015; Khan et al. 2014). The average crystallite size of G1 and G2 nanoparticles is found to be 30 and 56 nm, respectively. The average size of the nanoparticles is calculated from the most intense peak corresponding to the (211) plane using the Scherrer formula.
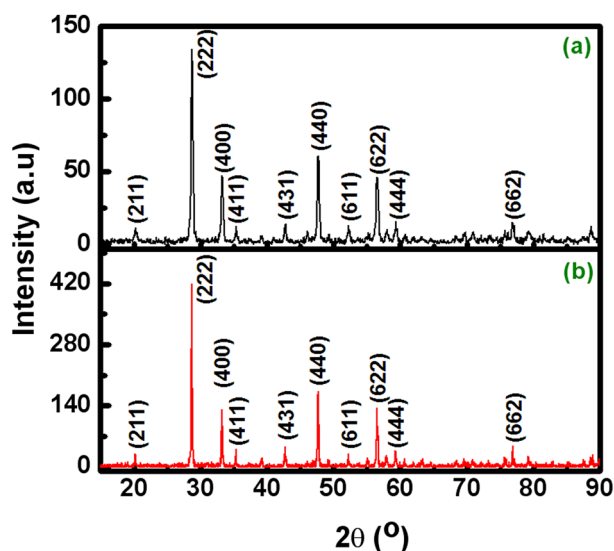
Figure 2 shows the (i) SAXS intensity distribution and (ii) particle size distribution of G1 and G2 nanoparticles, respectively. The average size of G1 and G2 nanoparticles is found to be 38 and 66 nm, respectively. Since the effective crystallite size (d_{eff}) of nanoparticles obtained using the Scherrer formula is smaller than its geometric diameter (d_g), i.e. $d_{eff} = (4/3)d_g$, the average size of the nanoparticles obtained using SAXS analysis is found to be larger than that obtained using XRD studies (Borchert et al. 2005).

Figure 3 shows the photographs of (a) silicone matrix without nanoparticles and (b) G1–25, (c) G1–2.5, (d) G2–25 and (e) G2–2.5 nanocomposite blocks, respectively. Silicone matrix without nanoparticles and G1–25, G1–2.5 and G2–2.5 nanocomposite blocks appear dark brown in colour, whereas G2–25 block appears brown in colour with a whitish tinge which may be attributed to the uniform distribution of G2 nanoparticles within the matrix. All the nanocomposite blocks are found to be flexible and
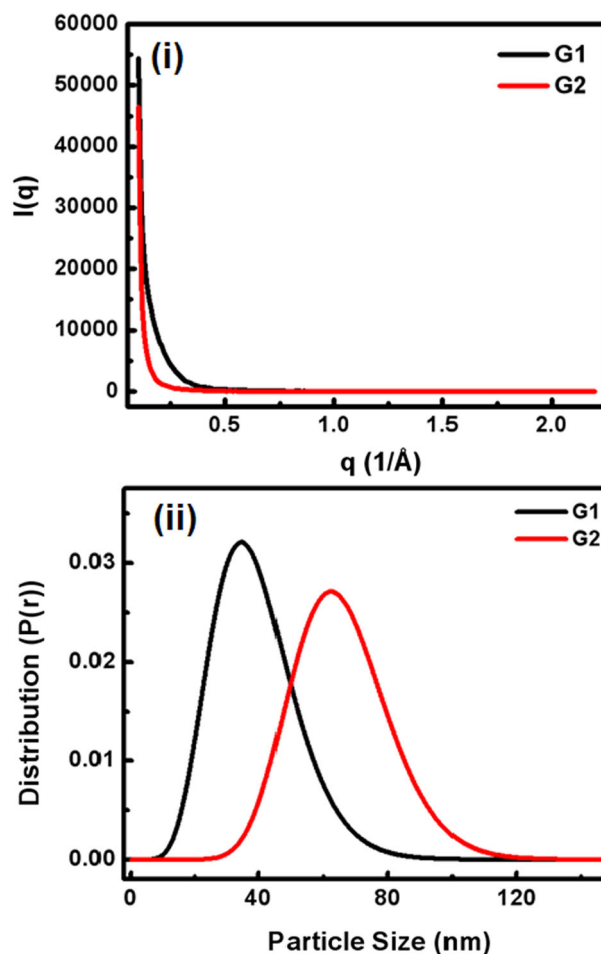
Fig. 1 XRD pattern of (a) G1 and (b) G2 nanoparticles

Fig. 2 i SAXS intensity distribution and **ii** particle size distribution of G1 and G2 nanoparticles, respectively
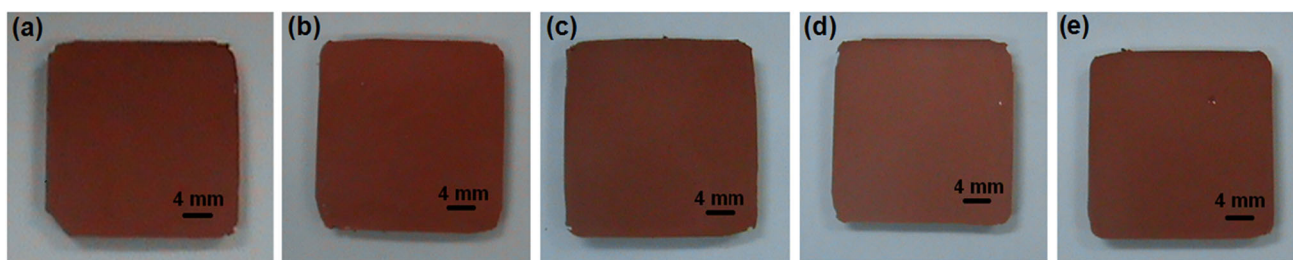
Fig. 3 Photographs of **a** silicone matrix without nanoparticles, **b** G1–25, **c** G1–2.5, **d** G2–25 and **e** G2–2.5 nanocomposite blocks, respectively
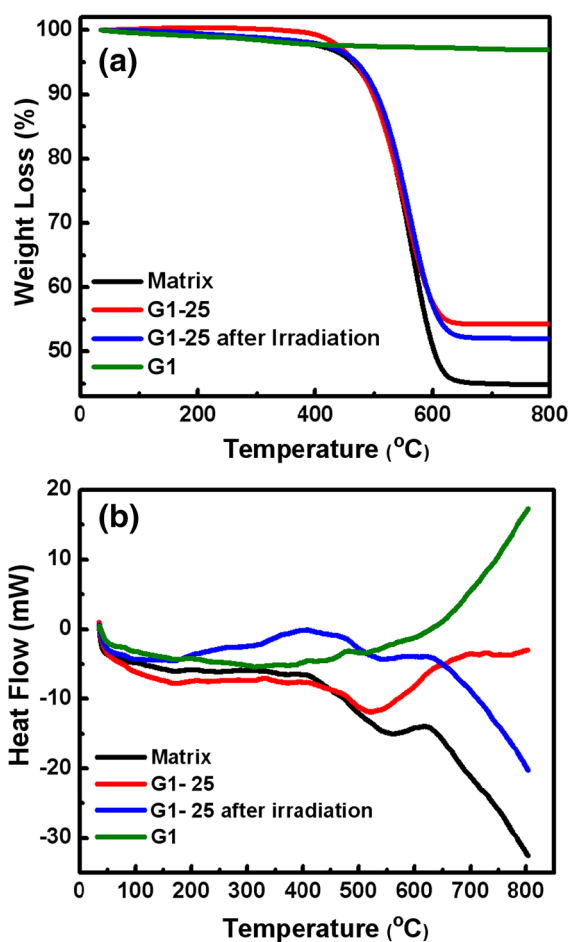

Fig. 4 **a** Weight loss curves and **b** DSC curves of the matrix, G1–25, G1–25 after irradiation and G1 nanoparticles, respectively

can be processed into different shapes with ease for various applications.

Figure 4 shows the (a) weight loss curves and (b) DSC curves of the matrix, G1–25, G1–25 after irradiation and G1 nanoparticles, respectively. The weight loss curve of the matrix shows a single-step weight reduction of 51% between 403 and 622 °C, corresponding to the degradation of silicone resin due to chain scission. Silicones possess siloxane or polysiloxane linkages consisting of silicon–oxygen bonds, which confer an inorganic nature to silicones. Silicones also

possess organic groups which impart hydrophobic property and are bonded via silicon–carbon linkages to the inorganic backbone (Dillon 1994). Thermoset silicone elastomer contains a cross-linking agent, a catalyst to accelerate vulcanization and an inhibitor to prevent premature reaction (Dillon 1994). Room temperature vulcanization systems (RTVs) are activated either by a catalyst which contains traces of metal or by moisture in ambient conditions (Dillon 1994). The Si–O bonds of silicones are known for their thermal stability (Wu et al. 2009). At high temperatures, the thermal degradation of silicone resin under inert atmosphere involves a two-step process, viz., unzipping reaction and a random main chain scission (Wu et al. 2009). The unzipping reaction involves breaking of cross-link chains associated with silanol terminal groups and the main chain scission involves the breaking of the backbone chain of the silicone network structure (Wu et al. 2009). The weight loss curve of G1–25 also shows a single-step weight reduction of 45% between 403 and 622 °C due to the degradation of silicone resin. The onset temperature of degradation occurs at the same temperature (403 °C in both matrix and in G1–25 nanocomposites) as that of the matrix without nanoparticles. This shows that the addition of nanofillers within the matrix does not deteriorate the thermal stability of the matrix. Similarly, the weight loss curve of G1–25 after irradiation shows a single-step weight reduction of 45% between 403 and 622 °C, further corroborating the absence of any change in thermal stability due to exposure to X-rays. The weight loss curve of G1 nanoparticles exhibits a weight reduction of 3% in the temperature range of 30–800 °C. A small weight loss of 3% exhibited by G1 nanoparticles is attributed to the loss of adsorbed moisture up to 190 °C and no significant weight loss was observed beyond 190 °C. The DSC curve of the matrix and G1–25 nanocomposites before and after X-ray irradiation exhibits a broad endothermic peak between 403 and 622 °C, corresponding to the degradation of the silicone resin. This further confirms the thermal stability of the nanoparticles. The DSC curve of G1 nanoparticles exhibits a gradual increase in heat flow beyond 600 °C, which may be attributed to the sintering of Gd_2O_3 nanoparticles.

Figure 5 shows the (a) weight loss curves and (b) DSC curves of matrix, G2–25, G2–25 after irradiation and G2 nanoparticles, respectively. The weight loss curve of the
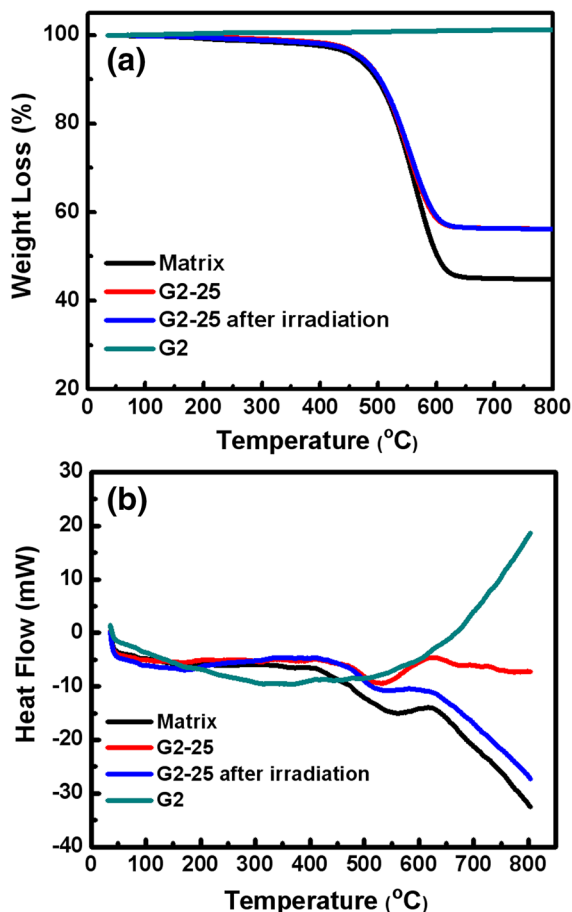
Fig. 5 a Weight loss curves and b DSC curves of the matrix, G2–25, G2–25 after irradiation and G2 nanoparticles, respectively

matrix exhibits a weight reduction of 51% between 403 and 690 °C, as described above (Wu et al. 2009). The weight loss curve of the G2–25 nanocomposite before and after X-ray irradiation exhibits a similar trend to that of nanocomposites containing G1 nanoparticles, with a weight reduction of 41% between 403 and 690 °C due to the degradation of silicone resin. The onset temperature of degradation of silicone resin is found to be the same (403 °C) before and after the addition of G2 nanofillers in the matrix and also before and after X-ray irradiation. This confirms the thermal stability of the nanocomposites containing G2 nanoparticles. The weight loss curve of bare G2 nanoparticles does not exhibit any significant weight loss in the temperature range of 30–800 °C. Heat flow curves of the matrix and G2–25 before and after X-ray irradiation exhibit an endothermic peak within the same temperature range of 403–622 °C. The heat flow curve of bare G2 nanoparticles exhibits an increase in the heat flow beyond 600 °C, which again may be attributed to the sintering of G2 nanoparticles.

Figure 6 shows the variation of mass attenuation coefficient of the matrix, G1–25, G1–2.5, G2–25 and G2–2.5
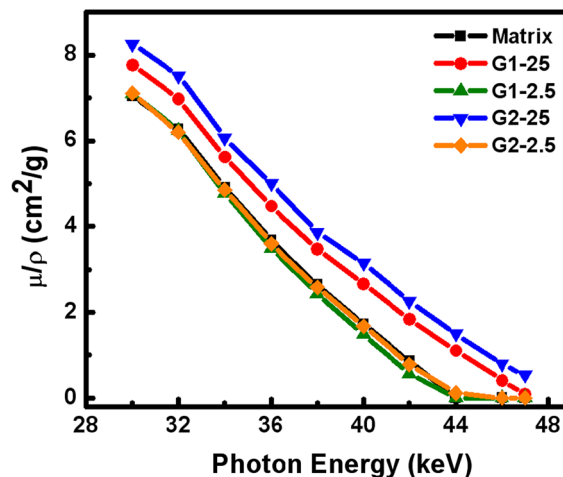

Fig. 6 Variation of mass attenuation coefficient of the matrix and G1–25, G1–2.5, G2–25 and G2–2.5 nanocomposite blocks as a function of X-ray photon energy

nanocomposite blocks as a function of X-ray photon energy. The attenuation of X-ray radiation by a material is given by an exponential attenuation law (Beer Lambert's Law) (Jackson and Hawkes 1981; Kelkar et al. 2015), as given below:

$$I = I_o e^{-\mu t}, \tag{3}$$

where, I is the intensity of transmitted X-rays, I_o the intensity of incident X-rays, μ the linear attenuation coefficient of the material and t the thickness of the attenuating material. This law is valid for the monochromatic X-ray source. Since linear attenuation coefficient varies with the density of the attenuating material, the attenuation of the prepared nanocomposite blocks is given in terms of the mass attenuation coefficient (μ_ρ). The mass attenuation coefficient is defined as the linear attenuation coefficient per unit density of the material (Davila et al. 2017; Ersundu et al. 2017). Nanocomposites containing 25 wt% G2 nanoparticles exhibit the highest mass attenuation coefficient compared to the rest of the prepared samples and is found to be in the range of 7.77–0.09 cm²/g for X-ray photon energy of 30–47 keV.

The X-ray photon energy ranges from 40 to 88 keV, known as the lead feeble absorbing area, is the commonly used photon energy range for medical diagnosis (Wang et al. 2015b). Lead-based nanocomposite shielding material, in addition to being toxic, exhibits good absorbing property above 88 keV and between 13 and 40 keV (Wang et al. 2015b). The absorption energy of k-shell of electron of lanthanides such as gadolinium ranges from 38.9 to 63.3 keV (Wang et al. 2015b), thus, covering a major portion of lead feeble absorbing area of X-ray photon energy. Hence, nanocomposites containing lanthanides such as gadolinium are of immense interest as a lead-free attenuating material.

The mass attenuation coefficient of the matrix and the nanocomposites is found to decrease gradually with an increase in X-ray photon energy from 30 to 47 keV. Nanocomposites containing 25 wt% G2 nanoparticles are found to exhibit a higher mass attenuation coefficient than nanocomposites containing G1 nanoparticles of equal concentration. A similar trend was observed for nanocomposites containing lower concentrations of G1 and G2 nanoparticles, where nanocomposites containing

Fig. 7 Percentage X-ray attenuation of the matrix and G1–25, G1–2.5, G2–25 and G2–2.5 nanocomposite blocks as a function of X-ray photon energy

2.5 wt% of G2 nanoparticles is found to exhibit a slightly higher mass attenuation coefficient than G1 nanocomposites of similar concentration.

Figure 7 shows the percentage X-ray attenuation of the matrix and G1–25, G1–2.5, G2–25 and G2–2.5 nanocomposite blocks as a function of X-ray photon energy. Nanocomposites containing G2 nanoparticles exhibit the highest percentage attenuation in the X-ray photon energy range of 30–47 keV. Attenuation of X-rays is not observed beyond 47 keV. Further enhancement of attenuation of X-rays by nanocomposites could be achieved by increasing the thickness of the nanocomposite blocks or by using multifillers or by functionalizing Gd_2O_3 nanoparticles for better dispersion in the matrix with increasing concentration. Table 1 shows the variation of mass attenuation coefficient and percentage attenuation of nanocomposites with different nanofiller loading, as a function of X-ray photon energy.

Half-value layer or HVL refers to the thickness of attenuating material sufficient enough to reduce the intensity of incident radiation by one-half, either by absorption or by scattering (Ersundu et al. 2017; Waly et al. 2016). The expression, $HVL = 0.693/\mu$ (Ersundu et al. 2017; Waly et al. 2016), relates HVL with the linear attenuation coefficient. Table 2 shows the half-value layer and linear attenuation coefficient of different nanocomposite blocks for X-rays of photon energy 30–47 keV. Lead equivalence is defined as the thickness of lead, which offers the same
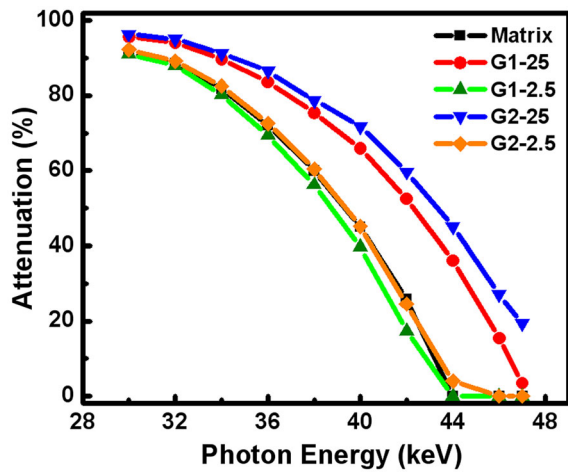
Table 1 Variation of mass attenuation coefficient and percentage attenuation of nanocomposites with different nanofiller loadings, as a function of X-ray photon energy

Samples	X-ray photon energy (keV)									
	30	32	34	36	38	40	42	44	46	47
	Mass attenuation coefficient in cm^2/g (percentage attenuation)									
Matrix	7.03 (91)	6.27 (89)	4.91 (82)	3.68 (72)	2.64 (60)	1.72 (45)	0.86 (26)	0 (0)	0 (0)	0 (0)
G1–25	7.77 (96)	6.97 (94)	5.62 (90)	4.48 (84)	3.47 (75)	2.66 (66)	1.84 (53)	1.11 (36)	0.41 (15)	0.09 (4)
G1–2.5	7.10 (91)	6.23 (88)	4.77 (80)	3.49 (69)	2.43 (56)	1.49 (40)	0.56 (17)	0 (0)	0 (0)	0 (0)
G2–25	8.26 (96)	7.52 (95)	6.07 (91)	5.00 (87)	3.86 (79)	3.15 (72)	2.26 (60)	1.50 (45)	0.79 (27)	0.54 (19)
G2–2.5	7.11 (92)	6.20 (89)	4.85 (83)	3.60 (73)	2.58 (60)	1.67 (45)	0.78 (25)	0.11 (4)	0 (0)	0 (0)

Table 2 Half-value layer and linear attenuation coefficient of different nanocomposite blocks for X-rays of photon energy 30–47 keV

| Samples	X-ray photon energy (keV)									
	30	32	34	36	38	40	42	44	46	47
	Half-value layer (cm)/linear attenuation coefficient (cm^{-1})									
Matrix	0.07/09.77	0.08/8.71	0.10/6.82	0.14/5.11	0.19/3.67	0.29/2.39	0.58/1.19	–/0	–/0	–/0
G1–25	0.06/12.11	0.06/10.86	0.08/8.76	0.10/6.97	0.13/5.40	0.17/4.15	0.24/2.87	0.40/1.72	1.08/0.64	5.03/0.14
G1–2.5	0.07/10.07	0.08/8.83	0.10/6.75	0.14/4.95	0.20/3.45	0.33/2.11	0.87/0.80	–/0	–/0	–/0
G2–25	0.05/12.74	0.06/11.60	0.07/9.36	0.09/7.72	0.12/5.96	0.14/4.86	0.20/3.49	0.30/2.31	0.57/1.22	0.84/0.83
G2–2.5	0.06/11.61	0.07/10.12	0.09/7.93	0.12/5.88	0.16/4.22	0.25/2.73	0.54/1.28	3.69/0.19	–/0	–/0
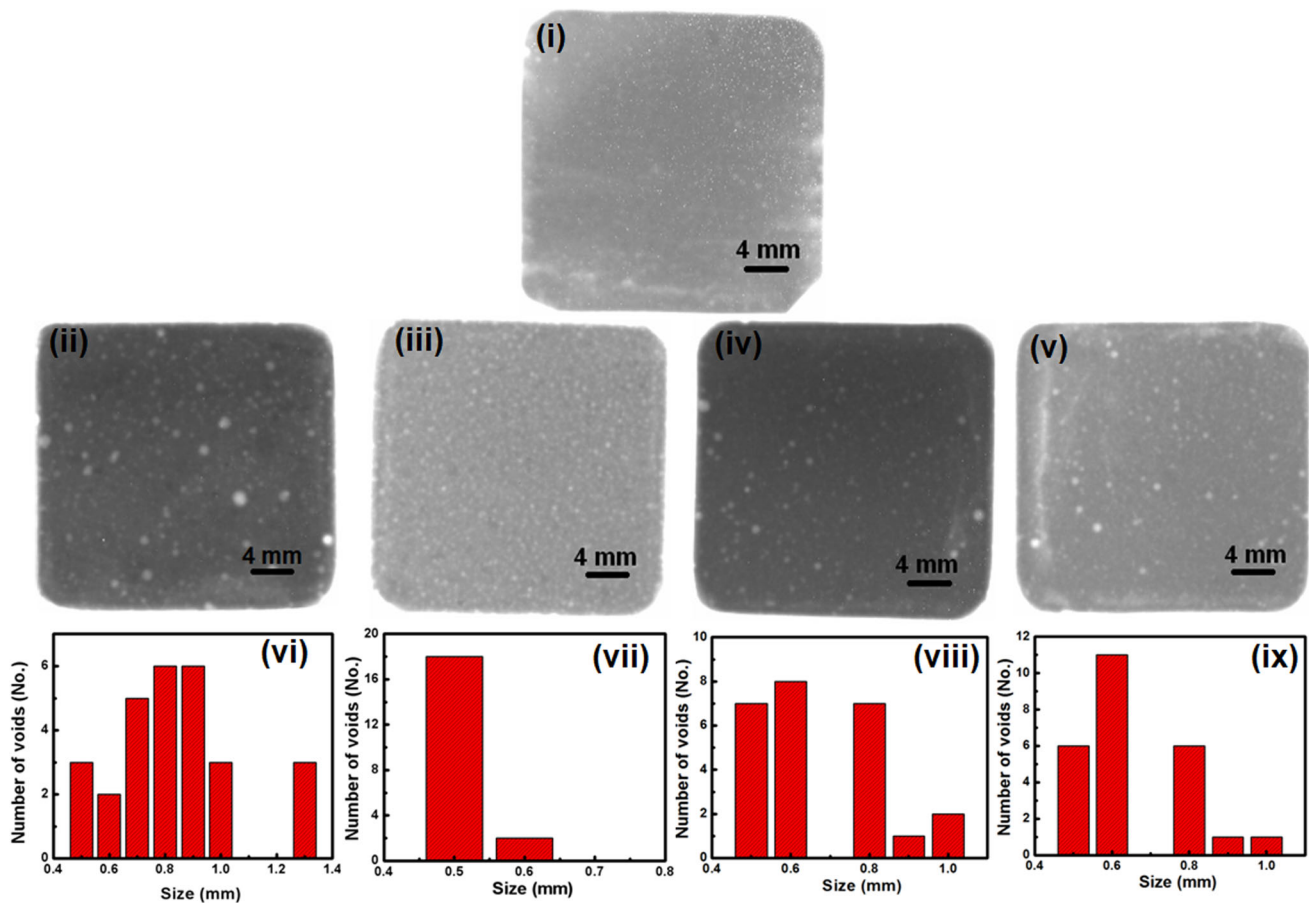
Fig. 8 Digital X-ray images of **i** the matrix and **ii** G1–25, **iii** G1–2.5, **iv** G2–25 and **v** G2–2.5, with the corresponding size distribution graph of voids in **vi** G1–25, **vii** G1–2.5, **viii** G2–25 and **ix** G2–2.5 nanocomposite blocks, respectively

attenuation as the material under consideration under similar conditions of irradiation (Nambiar et al. 2013; Scuderi et al. 2006). Thus, it is a standard reference for non-lead shielding material (Nambiar et al. 2013; Scuderi et al. 2006). The lead equivalence of nanocomposites containing G1 and G2 nanoparticles (25 wt%) at X-ray photon energy of 40 keV is found to be 0.094 and 0.08 mm, respectively.

Figure 8 shows the digital X-ray images of (i) the matrix, (ii) G1–25, (iii) G1–2.5, (iv) G2–25 and (v) G2–2.5, with the corresponding size distribution graphs of voids in (vi) G1–25, (vii) G1–2.5, (viii) G2–25 and (ix) G2–2.5 nanocomposite blocks, respectively. The white spots on the matrix are the X-ray transparent region. These spots correspond to voids within the matrix caused due to poor dispersibility of G1 and G2 nanoparticles in RTV silicone resin (Dong et al. 2011; Yasmin et al. 2003), which leads to nanoparticle-rich and nanoparticle-poor regions. The average diameter of these voids in nanocomposites containing G1 nanoparticles at concentrations of 25 and 2.5 wt% is found to be 0.95 and 0.5 μm, respectively. Similarly, the average diameter of the voids in

nanocomposites containing G2 nanoparticles at concentrations of 25 and 2.5 wt% is found to be the same (∼ 0.6 μm). It is observed that the size of microvoids in nanocomposites containing G1 nanoparticles is larger than that of nanocomposites containing G2 nanoparticles at a higher concentration of nanofiller (25 wt%). At lower concentration of nanofiller loading (2.5 wt%), the size of the microvoid is slightly smaller in case of nanocomposites containing G1 nanoparticles than that of nanocomposites containing G2 nanoparticles. This shows that G1 nanoparticles exhibit a concentration-dependent dispersibility in silicone resin. As the concentration of G1 nanoparticles increases in the matrix, the size of the microvoid increases, which is attributed to the pulling-out effect of nanoparticles due to low interfacial interaction between the nanofiller and silicone resin (Dong et al. 2011; Yasmin et al. 2003). Such microvoids could be avoided by functionalizing the nanoparticles with suitable functional groups. Silicone matrix without nanoparticles does not show such voids, thus confirming the role of interfacial interaction between the nanofiller and the matrix in void formation. The X-ray radiograph of the nanocomposite
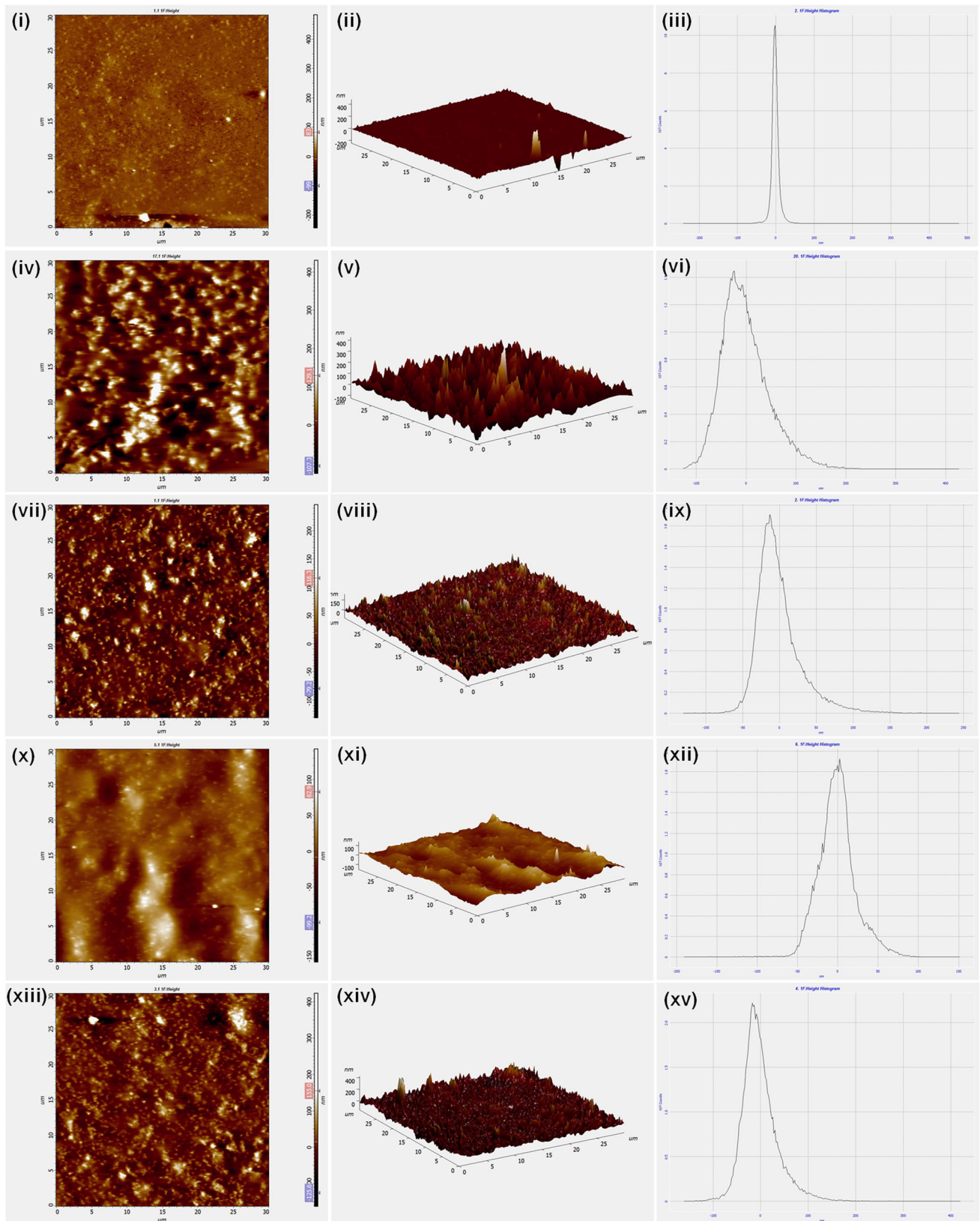
Fig. 9 AFM two-dimensional top surface topography, 3D image and surface roughness histogram of **i–iii** the matrix and **iv–vi** G1–25, **vii–ix** G1–2.5, **x–xii** G2–25 and **xiii–xv** G2–2.5 nanocomposite blocks, respectively

does not show the distribution of nanofiller within the polymer matrix due to its limitation in the detection of smaller-sized nanoparticles.

Figure 9 shows the AFM two-dimensional top surface topography, 3D image and surface roughness histogram of (i–iii) the matrix and (iv–vi) G1–25, (vii–ix) G1–2.5, (x–xii) G2–25 and (xiii–xv) G2–2.5 nanocomposite blocks, respectively. The AFM image of the matrix, as shown in Fig. 9i, exhibits a smooth surface with a roughness of 7 nm. The 3D image of the top surface of the matrix and the roughness histogram are shown in Fig. 9ii, iii, respectively. The AFM topography image of nanocomposites containing Gd_2O_3 nanoparticles of size 30 nm (G1) at 25 wt%, its 3D image and roughness histogram are shown in Fig. 9iv–vi,

respectively. The surface roughness of nanocomposites containing Gd_2O_3 nanoparticles of size 30 at 25 wt% is found to be 37 nm. Similarly, the AFM image, 3D representation and surface histogram of nanocomposites containing Gd_2O_3 nanoparticles of size 30 at 2.5 wt% are shown in Fig. 9vii–ix, respectively, with a surface roughness of 22 nm. Thus, the surface roughness of nanocomposites is found to increase with an increase in the concentration of G1 nanofillers. The AFM topography image, 3D image and roughness histogram of nanocomposites containing Gd_2O_3 nanoparticles of size 56 nm (G2) at 25 and 2.5 wt% are shown in Fig. 9x–xii and xiii–xv, respectively. The surface roughness of nanocomposites containing Gd_2O_3 of size 56 nm at a concentration of 25 and 2.5 wt% is found to be 17
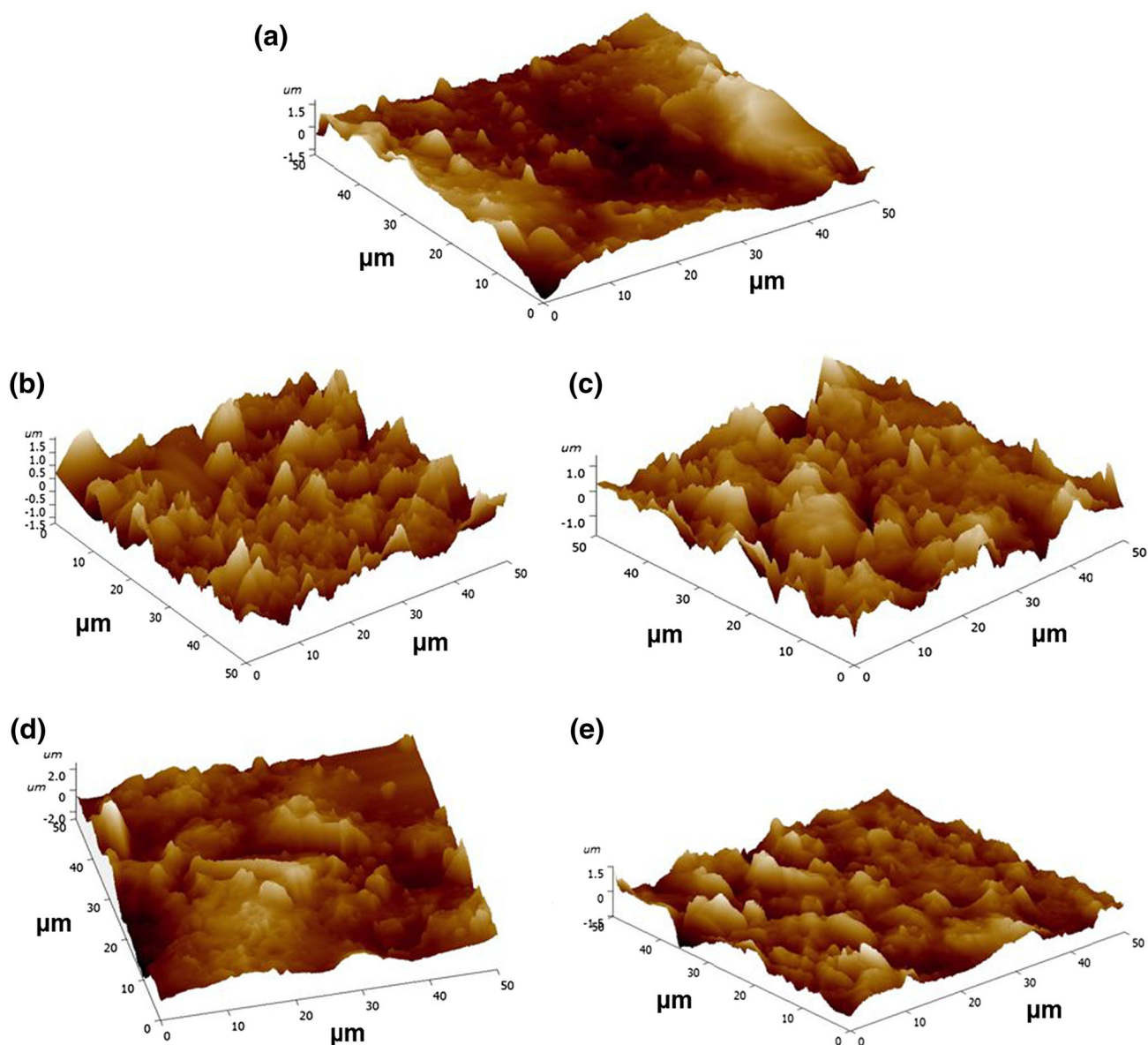

Fig. 10 AFM 3D topography image of cross section of **a** the matrix and **b** G1–25, **c** G1–2.5, **d** G2–25 and **e** G2–2.5 nanocomposite blocks
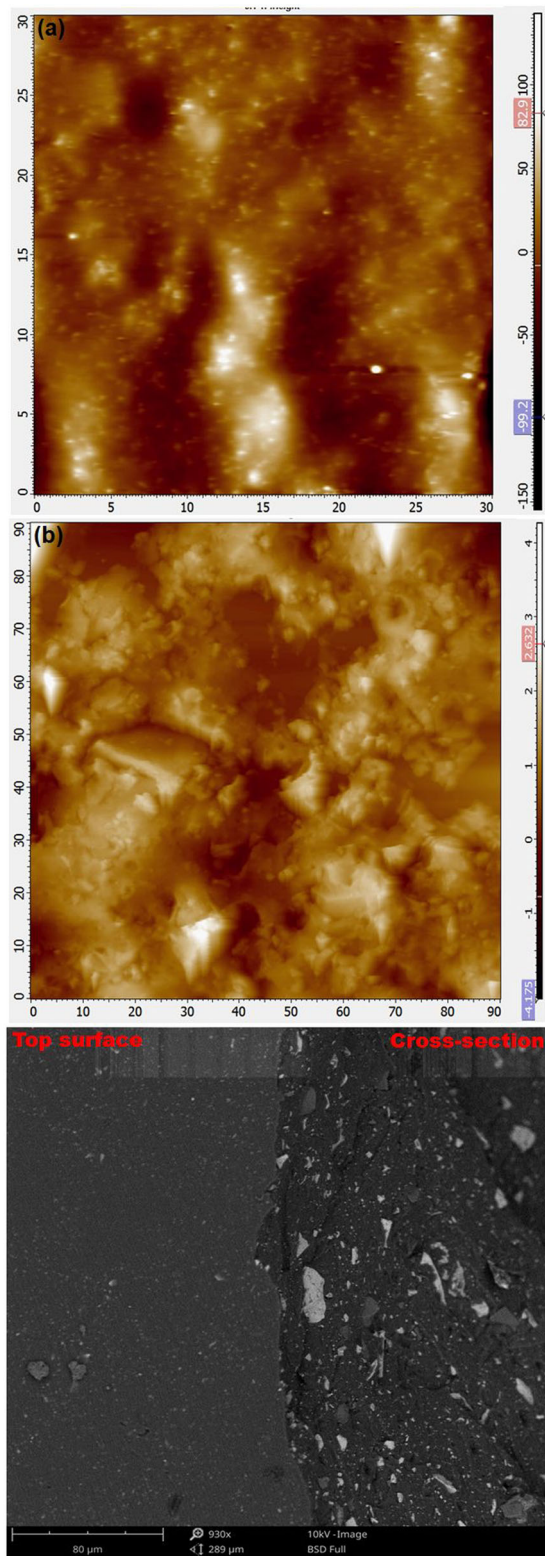
Fig. 11 a, **b** The AFM top surface topography and cross-sectional image of the G2–25 nanocomposite (X–Y unit in μm), and the SEM image of the top surface (left) and cross section (right) of the G2–25 nanocomposite, respectively

and 28 nm, respectively. Nanocomposite containing Gd_2O_3 nanoparticles of size 56 nm is found to exhibit a smoother surface at a higher (25 wt%) concentration than at a lower (2.5 wt%) concentration. This shows that nanocomposites containing Gd_2O_3 nanoparticles of size 30 nm at a concentration of 25 wt% exhibit a higher surface roughness than nanocomposites containing Gd_2O_3 of size 56 nm of similar concentration, attributing to the low attenuation property of G1-based nanocomposites. The surface roughness of nanocomposites containing 30 nm-size Gd_2O_3 nanoparticles, further, corroborates the pulling-out effect of these nanofillers.

Figure 10 shows the AFM 3D topography image of the cross section of (a) the matrix and (b) G1–25, (c) G1–2.5, (d) G2–25 and (e) G2–2.5 nanocomposite blocks. The AFM images of the cross section of nanocomposites exhibit exfoliated-type surface feature which may be attributed to the extent of interfacial interaction between the matrix and the nanofillers. Such surface feature is more prominent in G1–25, G1–2.5 and G2–2.5 nanocomposites than in G2–25 nanocomposites, which is in accordance with the AFM images of the top surface (uncleaved sample) morphology of the nanocomposite blocks. This further confirms a greater degree of interaction between the matrix and Gd_2O_3 nanoparticles of size 56 nm than that between the matrix and Gd_2O_3 nanoparticles of size 30 nm.

Figure 11a, b shows the AFM top surface topography and cross-sectional image of G2–25 nanocomposites, and the SEM image of the top surface (left) and the cross section (right) of G2–25 nanocomposites, respectively. The AFM and SEM images of G2–25 nanocomposite blocks, which exhibit the highest X-ray attenuation in comparison with other studied samples, further confirm the uniform distribution of nanofillers in its matrix.

Conclusion

We have successfully prepared nanocomposites containing Gd_2O_3 nanoparticles of two different sizes (30 and 56 nm) at concentrations of 25 and 2.5 wt%. The weight loss and heat flow curves of nanocomposites before and after the addition of nanofillers exhibit the degradation of the matrix in the temperature range of 403–622 °C, thus confirming the thermal stability of these materials up to ∼ 403 °C. Hence, the addition of nanofillers to the silicone matrix does not reduce the degradation temperature of the silicone matrix.

X-ray attenuation studies show that nanocomposites containing nanoparticles of size 56 nm exhibit better attenuation than nanocomposites containing nanoparticles

of size 30 nm due to a better interfacial interaction between the larger-sized nanofiller and the silicone matrix. The weak interfacial interaction between 30 nm-size nanofiller and the matrix results in the development of voids due to the pulling out of nanofillers and its aggregation in the matrix. The average diameter of these voids in nanocomposites containing nanoparticles of size 30 nm at concentrations of 25 and 2.5 wt% is found to be 0.95 and 0.5 μm, respectively. Similarly, the average diameter of the voids is found to be the same (0.6 μm) in nanocomposites containing 56 nm-size nanoparticles at concentrations of 25 and 2.5 wt%. The average size of the voids in nanocomposites containing 30-size nanofiller is larger than that of nanocomposites containing 56 nm-size nanofiller at a higher concentration of nanofiller loading (25 wt%). G1 nanofillers exhibit a concentration-dependent pulling-out effect and aggregation. These voids allow the X-rays to pass through the matrix, thereby reducing the overall X-ray attenuation property of the nanocomposites. The surface roughness of the nanocomposites obtained from AFM images further confirms the low interfacial interaction between the polymer matrix and 30 nm-size nanofillers. The percentage attenuation of nanocomposites containing nanoparticles of size 56 nm is found to be in the range of 96–19% for X-ray photon energies of 30–47 keV. Thus, our results show that nanocomposites containing Gd_2O_3 nanoparticles of size 56 nm may find application as an X-ray opaque fabric material, offering an alternate to toxic lead-based radiopaque fabric.

References

Abdulla R, Fidha M, Rao BHS, Kudkuli J, Rekha PD, Sharma SD (2015) Attenuation of ^{60}Co gamma rays by barium acrylic resin composite shields. Radiat Prot Environ 38:151–153. https://doi.org/10.4103/0972-0464.176157

Abdullah MM, Rahman MM, Bouzid H, Faisal M, Khan SB, Sayari SAA, Ismail AA (2015) Sensitive and fast response ethanol chemical sensor based on as-grown Gd_2O_3 nanostructures. J Rare Earth 33:214–220. https://doi.org/10.1016/S1002-0721(14)60405-1

Adliene D, Griskonis E, Vaiciunaite N, Nalivaiko RP (2015) Evaluation of new transparent tungsten containing nanocomposites for radiation protection screens. Radiat Prot Dosim 165:406–409. https://doi.org/10.1093/rpd/ncv072

Ahren M et al (2012) A simple polyol-free synthesis route to Gd_2O_3 nanoparticles for MRI applications: an experimental and theoretical study. J Nanopart Res 14:1006. https://doi.org/10.1007/s11051-012-1006-2

Akbulut S, Sehhatigdiri A, Eroglu H, Celik S (2015) A research on the radiation shielding effects of clay, silica fume and cement samples. Radiat Phys Chem 117:88–92. https://doi.org/10.1016/j.radphyschem.2015.08.003

Ambika MR, Nagaiah N, Suman SK (2016) Role of bismuth oxide as a reinforcer on gamma shielding ability of unsaturated polyester based polymer composites. J Appl Polym Sci. https://doi.org/10.1002/app.44657 **(In press)**

Aral N, Nergis FB, Candan C (2016) An alternative X-ray shielding material based on coated textiles. Text Res J 86:803–811. https://doi.org/10.1177/0040517515590409

Bhattacharyya S, Agrawal DC (1995) Preparation of tetragonal ZrO_2–Gd_2O_3 powders. J Mater Sci 30:1495–1499. https://doi.org/10.1007/BF00375254

Borchert H, Shevchenko EV, Robert A, Mekis I, Kornowski A, Grubel G, Weller H (2005) Determination of nanocrystal sizes: a comparison of TEM, SAXS and XRD studies of highly monodisperse $CoPt_3$ particles. Langmuir 21:1931–1936. https://doi.org/10.1021/la0477183

Chen Z (1996) Effects of gadolinia and alumina addition on the densification and toughening of silicon carbide. J Am Ceram Soc 79:530–532. https://doi.org/10.1111/j.1151-2916.1996.tb08160.x

Davila HO, Merchan JAD, Carrillo HRV, Ovalle SAM (2017) Assessment of the effectiveness of attenuation of Pb aprons by using TLD dosimetry and Monte Carlo calculations. Appl Radiat Isot. https://doi.org/10.1016/j.apradiso.2017.05.012 **(In press)**

Dillon ME (1994) Silicone and poly(tetrafluoroethylene) interpenetrating polymer networks-Brief history, summary of recent developments, and discussion of applications. In: Klempner D, Sperling LH, Utracki LA (eds) interpenetrating polymer networks, vol 239. Advances in Chemistry. American Chemical Society, Washington, DC, pp 393–404

Dong Y, Chaudhary D, Ploumis C, Lau KT (2011) Correlation of mechanical performance and morphological structures of epoxy micro/nanoparticulate composites. Compos A 42:1483–1492. https://doi.org/10.1016/j.compositesa.2011.06.015

Dosev D, Nichkova M, Liu M, Guo B, Liu G, Hammock BD, Kennedy IM (2006) Application of luminescent Eu:Gd_2O_3 nanoparticles to the visualization of protein micropatterns. J Biomed Opt 10:064006. https://doi.org/10.1117/1.2136347

Duc GL et al (2011) Toward an image-guided microbeam radiation therapy using gadolinium-based nanoparticles. ACS Nano 5:9566–9574. https://doi.org/10.1021/nn202797h

Ersundu MC, Ersundu AE, Sayyed MI, Lakshminarayana G, Aydin S (2017) Evaluation of physical, structural properties and shielding parameters for K_2O–WO_3–TeO_2 glasses for gamma ray shielding applications. J Alloys Compd 714:278–286. https://doi.org/10.1016/j.jallcom.2017.04.223

Flora G, Gupta D, Tiwar A (2012) Toxicity of lead: a review with recent updates. Interdiscip Toxicol 5:47–58. https://doi.org/10.2478/v10102-012-0009-2

Fontainha CCP, Neto ATB, Santos AP, Faria LOD (2016) P(VDF–TrFE)/ZrO_2 polymer-composites for X-ray shielding. Mater Res 19:426–433. https://doi.org/10.1590/1980-5373-MR-2015-0576

Fortin MA et al (2007) Polyethylene glycol-covered ultra-small Gd_2O_3 nanoparticles for positive contrast at 1.5 T magnetic resonance clinical scanning. Nanotechnology 18:395501. https://doi.org/10.1088/0957-4484/18/39/395501

Fujimori T et al (2011) Enhanced X-ray shielding effects of carbon nanotubes. Mater Express 1:273–278. https://doi.org/10.1166/mex.2011.1043

Gayathri T, Sundaram NM, Kumar RA (2015) Gadolinium oxide nanoparticles for magnetic resonance imaging and cancer theranostics. J Bionanosci 9:1–15. https://doi.org/10.1166/jbns.2015.1325

Gunduz G, Uslu I (1996) Powder characteristics and microstructure of uranium dioxide and uranium dioxide-gadolinium oxide fuel. J Nucl Mater 231:113–120. https://doi.org/10.1016/0022-3115(96)00349-2

Hussein GAM (1994) Formation, characterization, and catalytic activity of gadolinium oxide. Infrared spectroscopic studies. J Phys Chem 98:9657–9664. https://doi.org/10.1021/j100089a047

Jackson DF, Hawkes DJ (1981) X-ray attenuation coefficients of elements and mixtures. Phys Rep 70:169–233. https://doi.org/10.1016/0370-1573(81)90014-4

Jamnezhad H, Jafari M (2016) Structure of Gd_2O_3 nanoparticles at high temperature. J Magn Magn Mater 408:164–167. https://doi.org/10.1016/j.jmmm.2016.02.041

Jayakumar S, Saravanan T, Philip J (2017) Thermal stability and X-ray attenuation studies of α-Bi_2O_3, β-Bi_2O_3 and Bi based nanocomposites for radiopaque fabrics. J Nanosci Nanotechnol. https://doi.org/10.1166/jnn.2017.15237 (in press)

Kelkar S, Boushey CJ, Okos M (2015) A method to determine the density of foods using X-ray imaging. J Food Eng 159:36–41. https://doi.org/10.1016/j.jfoodeng.2015.03.012

Khan SA, Gambhir S, Ahmad A (2014) Extracellular biosynthesis of gadolinium oxide (Gd_2O_3) nanoparticles, their biodistribution and bioconjugation with the chemically modified anticancer drug taxol. Beilstein J Nanotechnol 5:249–257. https://doi.org/10.3762/bjnano.5.27

Kim Y, Park S, Seo Y (2015) Enhanced X-ray shielding ability of polymer-nonleaded metal composites by multilayer structuring. Ind Eng Chem Res 54:5968–5973. https://doi.org/10.1021/acs.iecr.5b00425

Kiran K (2015) MSA-capped gold nanoparticle-supported alumina for the determination of Pb and Cd in various environmental water samples. Appl Nanosci 5:795–800. https://doi.org/10.1007/s13204-014-0377-3

Kusiak E, Zaborski M (2012) Characteristic of natural rubber composites absorbing X-radiation. Compos Interface 19:433–439. https://doi.org/10.1080/15685543.2012.759815

La LBT, Leong YK, Leatherday C, Au PI, Hayward KJ, Zhang LC (2016) X-ray protection, surface chemistry and rheology of ball-milled submicron Gd_2O_3 aqueous suspension. Colloids Surf A 501:75–82. https://doi.org/10.1016/j.colsurfa.2016.04.058

Li Z, Chen S, Nambiar S, Sun Y, Zhang M, Zheng W, Yeow JTW (2016) PMMA/MWCNT nanocomposite for proton radiation shielding applications. Nanotechnology 27:234001. https://doi.org/10.1088/0957-4484/27/23/234001

Li R, Gu Y, Wang Y, Yang Z, Li M, Zhang Z (2017) Effect of particle size on gamma radiation shielding property of gadolinium oxide dispersed epoxy resin matrix composite. Mater Res Express 4:035035. https://doi.org/10.1088/2053-1591/aa6651

Mao Y, Zhi X, Hu S, Ma X, Wen S, Fong H, Liu L (2015) Preparation of Gd_2O_3 nano-flakes and fabrication/evaluation of their X-ray shielding rubber nanocomposites with improved mechanical properties. J Compos Mater 49:1989–1994. https://doi.org/10.1177/0021998314541309

Miladi I et al (2015) Combining ultrasmall gadolinium-based nanoparticles with photon irradiation overcomes radioresistance of head and neck squamous cell carcinoma. Nanomedicine 11:247–257. https://doi.org/10.1016/j.nano.2014.06.013

Mowat P et al (2011) In vitro radiosensitizing effects of ultrasmall gadolinium based particles on tumour cells. J Nanosci Nanotechnol 11:7833–7839. https://doi.org/10.1166/jnn.2011.4725

Nambiar S, Osei EK, Yeow JTW (2013) Polymer nanocomposite-based shielding against diagnostic X-rays. J Appl Polym Sci 127:4939–4946. https://doi.org/10.1002/app.37980

Perevalov TV, Dolbak AE, Shvets VA, Gritsenko VA, Asanova TI, Erenburg SB (2014) Atomic and electronic structure of gadolinium oxide Eur Phys. J Appl Phys 65:10702. https://doi.org/10.1051/epjap/2013130239

Ramalho J, Semelka RC, Ramalho M, Nunes RH, AlObaidy M, Castillo M (2016) Gadolinium-based contrast agent accumulation and toxicity: an update. Am J Neuroradiol 37:1192–1198. https://doi.org/10.3174/ajnr.A4615

Rancoule C, Magne N, Vallard A, Guy JB, Lafrasse CR, Deutsch E, Chargari C (2016) Nanoparticles in radiation oncology: from bench-side to bedside. Cancer Lett 375:256–262. https://doi.org/10.1016/j.canlet.2016.03.011

Rima W et al (2013) Internalization pathways into cancer cells of gadolinium-based radiosensitizing nanoparticles. Biomaterials 34:181–195. https://doi.org/10.1016/j.biomaterials.2012.09.029

Rogosnitzky M, Branch S (2016) Gadolinium-based contrast agent toxicity: a review of known and proposed mechanisms. Biometals 29:365–376. https://doi.org/10.1007/s10534-016-9931-7

Roux S et al (2010) Multifunctional gadolinium oxide nanoparticles: towards image-guided therapy. Imaging Med 2:211–223. https://doi.org/10.2217/iim.10.5

Sambhudevan S, Shankar B, Saritha A, Joseph K, Philip J, Saravanan T (2017) Development of X-ray protective garments from rare earth-modified natural rubber composites. J Elastom Plast 49:527–544. https://doi.org/10.1177/0095244316676866c

Scuderi GJ, Brusovanik GV, Campbell DR, Henry RP, Kwon B, Vaccaro AR (2006) Evaluation of non-lead-based protective radiological material in spinal surgery. Spine J 6:577–582. https://doi.org/10.1016/j.spinee.2005.09.010

Stefancikova L et al (2016) Effect of gadolinium-based nanoparticles on nuclear DNA damage and repair in glioblastoma tumor cells. J Nanobiotechnol 14:63. https://doi.org/10.1186/s12951-016-0215-8

Thibeault SA, Kang JH, Sauti G, Park C, Fay CC, King GC (2015) Nanomaterials for radiation shielding. Mater Res Soc Bull 40:836–841. https://doi.org/10.1557/mrs.2015.225

Waly ESA, Fusco MA, Bourham MA (2016) Gamma-ray mass attenuation coefficient and half value layer factor of some oxide glass shielding materials. Ann Nucl Energy 96:26–30. https://doi.org/10.1016/j.anucene.2016.05.028

Wang F, Peng E, Zheng B, Li SFY, Xue JM (2015a) Synthesis of water-dispersible Gd_2O_3/GO nanocomposites with enhanced MRI T1 relaxivity. J Phys Chem C 119:23735–23742. https://doi.org/10.1021/acs.jpcc.5b06037

Wang H et al (2015b) Preparation and radiation shielding properties of Gd_2O_3/PEEK composites. Polym Compos 36:651–659. https://doi.org/10.1002/pc.22983

Wu C, Li W, Gao D, Jia M (2009) Study of resistance of silicone resin to heat and irradiation. Polym Plast Technol Eng 48:1094–1100. https://doi.org/10.1080/03602550903147213

Yasmin A, Abot JL, Daniel IM (2003) Processing of clay/epoxy nanocomposites by shear mixing. Scr Mater 49:81–86. https://doi.org/10.1016/S1359-6462(03)00173-8

Zhou L et al (2017) Size-tunable Gd_2O_3@Albumin nanoparticles conjugating Chlorin e6 for magnetic resonance imaging-guided photo-induced therapy. Theranostics 7:764–774. https://doi.org/10.7150/thno.15757

Publisher's Note

Springer Nature remains neutral with regard to jurisdictional claims in published maps and institutional affiliations.